Supplementary Information for

Evidence for vacuum-enhanced superconductivity in $NbSe_2$

Zheyan Wang[1,2,3], Gabriel Cardoso[4], Liu Yang[4,5], Xun Gong[1,2,3], Chi Zhang[1,2,3], Yufei Zhu[2,6], Dongbo Zhang[1,2,3], Nan Pan[2,3], Hongbing Cai[2,3], Yong P. Chen[7,8,9], Qing-Dong Jiang[2,4,5,*], Guanghui Cheng[1,3,8,10,*], Frank Wilczek[4,5,11,12,13,*], Changgan Zeng[1,2,3,*]

[1]Department of Physics, University of Science and Technology of China, Hefei 230026, China.

[2]Hefei National Laboratory, Hefei 230088, China.

[3]International Center for Quantum Design of Functional Materials (ICQD), Hefei National Research Center for Physical Sciences at the Microscale, University of Science and Technology of China, Hefei 230026, China.

[4]Tsung-Dao Lee Institute, Shanghai Jiao Tong University, Shanghai 201210, China.

[5]School of Physics and Astronomy, Shanghai Jiao Tong University, Shanghai 200240, China.

[6]Wilczek Quantum Center, Shanghai Institute for Advanced Studies, University of Science and Technology of China, Shanghai 201315, China.

[7]Institute for Materials Research (IMR), Tohoku University, Sendai 980-8577, Japan.

[8]WPI Advanced Institute for Materials Research (AIMR), Tohoku University, Sendai 980-8577, Japan.

[9]Institute of Physics and Astronomy and Villum Centers for Hybrid Quantum Materials and Devices, Aarhus University, 8000 Aarhus-C, Denmark.

[10]Frontier Research Institute for Interdisciplinary Sciences (FRIS), Tohoku University, Sendai 980-8578, Japan.

[11]Department of Physics, Stockholm University, Stockholm 10691, Sweden.

[12]Department of Physics and Origins Project, Arizona State University, Tempe, Arizona 25287, USA.

[13]Center for Theoretical Physics, Massachusetts Institute of Technology, Cambridge, Massachusetts 02139, USA.

*Corresponding authors. Emails: qingdong.jiang@sjtu.edu.cn; cghui@ustc.edu.cn; wilczek@mit.edu; cgzeng@ustc.edu.cn.

CONTENTS

Supplementary Note 1. Rationale for the chosen cavity

Supplementary Note 2. Discussion on the chosen 12-layer $NbSe_2$ and its dimensionality

Supplementary Note 3. Method of the electromagnetic simulations and determination of ε_s and V_{eff}

Supplementary Note 4. Spatial localization of the field and its impact on superconductivity

Supplementary Note 5. Extraction of the critical temperature T_c

Supplementary Note 6. Dependence on the thickness of Al_2O_3 spacer

Supplementary Note 7. Dependence on the thickness of $NbSe_2$

Supplementary Note 8. Replacement of Al_2O_3 dielectric spacer with HfO_2

Supplementary Note 9. Ginzburg-Landau theory for the coupled superconductor-cavity system

Supplementary Note 10. Extraction of Q and its impact on T_c modulation

Supplementary Note 11. Influence of the dielectric environment on T_c modulation

Supplementary Note 12. Discussion based on the sub-wavelength cavity theory

Supplementary Note 13. Discussion based on the microscopic picture of polaritonic coupling

Supplementary Note 14. Strategies for amplifying cavity-enhanced superconductivity

Supplementary Figure 1. Extraction of transition temperatures

Supplementary Figure 2. Dependence on the thickness of Al_2O_3

Supplementary Figure 3. Dependence on the thickness of $NbSe_2$

Supplementary Figure 4. Control experiment with HfO_2 spacer

Supplementary Figure 5. Bare ψ propagator

Supplementary Figure 6. Tadpole correction to the propagator

Supplementary Figure 7. Second-order diagram correction to the propagator

Supplementary Figure 8. Frequency-dependent superconductivity enhancement for different Q values

Supplementary Note 1. Rationale for the chosen cavity

The choice of the cavity was guided by four main considerations: (1) The sub-wavelength split-ring resonator can achieve a high field enhancement. The vacuum field fluctuation amplitude is estimated to be ~260 V/m, almost four orders of magnitude stronger than that of the free space (~0.43 V/m) for the same frequency. Such field boosting can significantly enhance the light-matter interaction. (2) The frequency of the split-ring cavity can be easily tuned to the resonance condition: the typical near-terahertz frequency of the cavity matches the energy of the superconducting fluctuation of $NbSe_2$ (see analysis of the resonance condition in the main text). (3) The planar split-ring architecture is compatible with the exfoliated layered materials, allowing for flexible alignment and integration. (4) As verified in earlier works[1,2], such split-ring cavity can enable effective coupling with electron systems.

Supplementary Note 2. Discussion on the chosen 12-layer $NbSe_2$ and its dimensionality

Very thin $NbSe_2$ flakes (e.g., monolayers, bilayers) are more susceptible to disorder, strain, and fabrication-induced degradation, which lead to strong inhomogeneity and intrinsic fluctuations of T_c. This poses a significant challenge for the systematic study of the relatively modest cavity-enhanced T_c. The possibly broadened superconducting transitions in few layers also complicate an accurate determination of T_c. In contrast, for 12-layer $NbSe_2$, we can reliably obtain sharp, uniform transitions with reproducible T_c, allowing high-precision transport measurements.

Based on the DFT calculations and ARPES measurements, the electronic structure of four-layer $NbSe_2$ is already very close to the bulk limit[3,4]. $NbSe_2$ with more than ten layers exhibits properties identical to those of the bulk, in terms of phonon modes[5], as well as charge density wave and superconductivity[6,7]. From this perspective, the 12-layer sample already lies within the bulk-like electronic regime. At the same time, the observation of BKT-like behavior in transport measurements (Extended Data Fig. 5) is not contradictory. The BKT transition reflects vortex-antivortex physics in the in-plane superconducting response, rather than the underlying electronic dimensionality. Since the thickness of the 12-layer sample (~8 nm) is comparable to the superconducting coherence length and much smaller than its penetration depth, phase fluctuations and quasi-two-dimensional vortex dynamics can naturally emerge near T_c, even though the electronic structure is already bulk-like.

From an application standpoint of the cavity, its relatively thick structure (~210 nm in height), together with the spatially broad field distribution (Extended Data Fig. 1), make it applicable to much thicker bulk superconductors as well.

Supplementary Note 3. Method of the electromagnetic simulations and determination of ε_s and V_{eff}

The field distributions in Extended Data Fig. 1 are obtained by finite-element simulations performed with Computer Simulation Technology (CST) Microwave Studio[1,8]. The metallic cavity is modeled as standard lossy gold from the material library. The substrate consists of 285-nm-thick SiO_2 on top of 675-μm-thick Si. $NbSe_2$ is modeled as a perfect electric conductor. The thin Al_2O_3 and hBN layers are omitted from the simulations to reduce the computational cost. The field distribution is obtained at the central height of the $NbSe_2$ layer.

The effective permittivity ε_s is defined as $\varepsilon_s \approx \left(\frac{f_{vac}}{f_{sub}}\right)^2$, where f_{vac} and f_{sub} are the cavity frequencies in vacuum and on substrate, respectively, and their values are obtained by electromagnetic simulations based on actual device geometry. Therefore, we can obtain $\varepsilon_s = 5.1$. The effective volume V_{eff} is defined as $V_{eff} = \frac{\int_{all\ space} \varepsilon |E(\boldsymbol{r})|^2 dV}{\max[\varepsilon |E(\boldsymbol{r})|^2]}$ in the standard way used in cavity quantum electrodynamics[9]. The field distribution in this expression is obtained by electromagnetic simulations based on actual device geometry, which yields $V_{eff} = 79\ \mu m^3$.

Supplementary Note 4. Spatial localization of the field and its impact on superconductivity

As shown in Extended Data Fig. 1b, the field is localized at the edge of the superconductor and may give rise to different T_c values for the edge and interior regions. However, transport measurements may not resolve this difference even if the edge and interior contribute differently. The conductance of the edge and interior can be viewed as a parallel circuit, in which the zero-resistance edge (presumably higher-T_c) may short-circuit the lower-T_c interior. As a result, one may still observe a single superconducting transition even in the presence of edge-interior difference.

On the other hand, the superconducting state is inherently nonlocal and phase coherent. Even if the cavity field is spatially concentrated near the edge, its effect is not necessarily restricted to that region. Physically, the edge and interior are coupled through the superconducting order parameter. Enhancement of superconductivity at the edge can propagate into the interior via well-established mechanisms such as proximity-induced pairing and Andreev processes. In addition, the superconducting phase must remain globally coherent, which imposes a constraint that couples different regions of the sample. As a result, a local modification of the pairing strength can influence the effective transition of the entire device, leading to a measurable T_c modulation even in regions where the field is weaker.

With the present transport geometry, fully isolating the edge contribution in experiments is challenging because the measured resistance is not a simple linear superposition of regions with different local T_c and current distributions. Here, we propose several strategies to isolate/quantify the edge effect: (1) Etching the superconductor flake to a width comparable to the edge-enhanced region (<100 nm), so that the entire flake is an effective “edge”; (2) Using local probes (e.g., scanning superconducting quantum interference device or scanning tunneling spectroscopy) to map the spatial variation of the superconducting gap. While this work provides clear global evidence of the cavity-induced superconductivity enhancement, a spatially resolved characterization would be an important next step.

Supplementary Note 5. Extraction of the critical temperature T_c

We determine the transition temperatures following the fitting method[10,11]. As shown in Supplementary Fig. 1, the central part of the transition is fitted linearly, and its intersections with the extrapolated zero-resistance and normal-resistance lines define T_c^{offset} and T_c^{onset}, respectively. The critical temperature T_c is determined as $T_c = \frac{(T_c^{\text{offset}}+T_c^{\text{onset}})}{2}$.

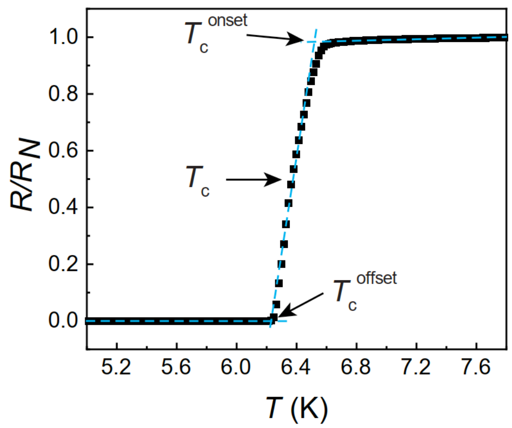

Supplementary Figure 1. Extraction of transition temperatures. The data points are from Fig. 1c of the main text. Three dashed lines represent the linear fits of the central part of the transition, the zero-resistance state and the normal-resistance state, respectively. Their intersections define T_c^{offset} and T_c^{onset}. The critical temperature T_c is determined as $T_c = \frac{(T_c^{\text{offset}}+T_c^{\text{onset}})}{2}$.

Supplementary Note 6. Dependence on the thickness of Al_2O_3 spacer

We have further studied the dependence on the thickness of Al_2O_3 spacer. As shown in Supplementary Fig. 3, T_c modulations are 1.0% and 1.2% for the 10-nm and 20-nm Al_2O_3 cases, respectively. This robustness of T_c modulation against Al_2O_3 thickness rules out the fabrication-related effects involving Al_2O_3 deposition, and also implies that slightly shifting the $NbSe_2$ position within the cavity gap (by 10 nm downward in this case) does not significantly alter the coupling between the cavity and $NbSe_2$.

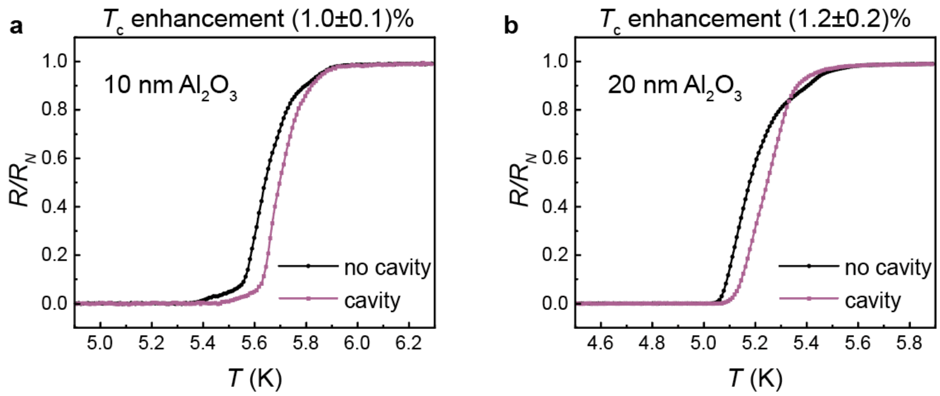

Supplementary Figure 2. Dependence on the thickness of Al_2O_3. Cavity-modulated superconductivity for devices with Al_2O_3 thicknesses of (**a**) 10 nm and (**b**) 20 nm. The cavity frequency is 0.92 THz. The $NbSe_2$ flakes have a thickness of 12 layers in both cases.

Supplementary Note 7. Dependence on the thickness of $NbSe_2$

We have investigated the dependence on the thickness of the superconductor. Supplementary Figure 3a-d shows cavity-enhanced superconductivity in devices with $NbSe_2$ thicknesses of 6, 8, 12, and 17 layers. The corresponding T_c enhancement as a function of layer number is summarized in Supplementary Fig. 3e. Note that all data points in this layer-number-dependent dataset were obtained from the same batch of devices with identical fabrication processes.

For thick $NbSe_2$ (8, 12, and 17 layers), the baseline T_c values (black curves in Supplementary Fig. 3b-d) are around 5.5 K-5.6 K, while the T_c enhancement remains nearly constant at around 1%. However, for 6-layer $NbSe_2$, the baseline T_c drops to around 4.1 K (black curve in Supplementary Fig. 3a), reflecting stronger superconducting fluctuations at reduced dimensionality. Simultaneously, T_c enhancement increases dramatically to 5.4%. Such enhanced superconducting fluctuations may strengthen the low-energy electromagnetic response of the superconducting film, thereby enabling more effective coupling to the cavity electromagnetic modes. This trend therefore provides further support for the cavity-based interpretation.

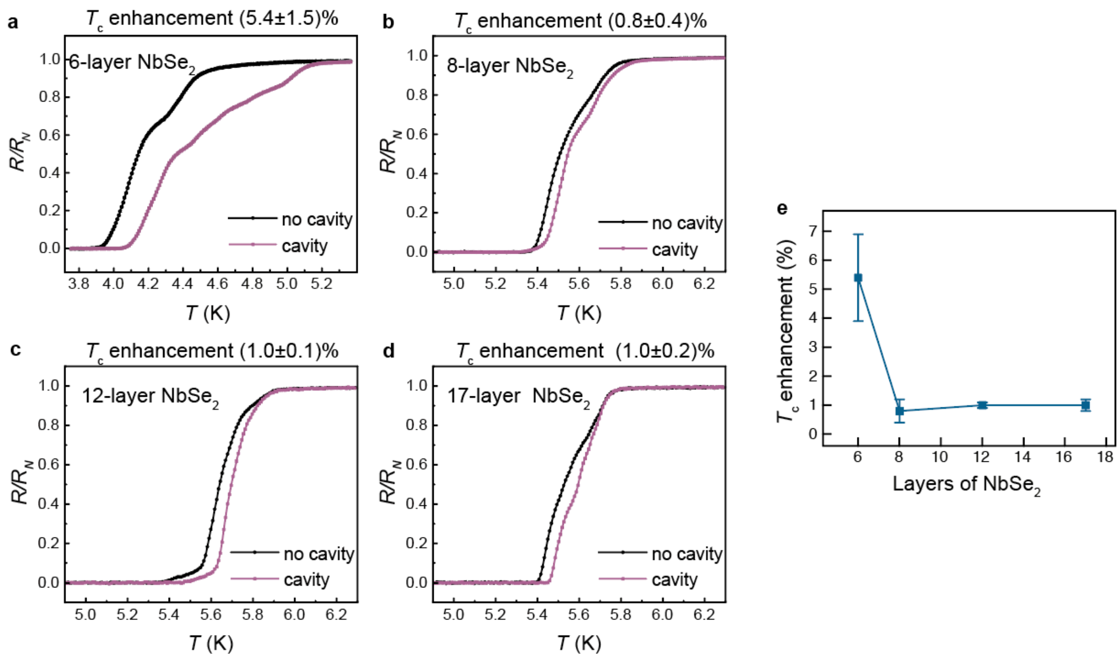

Supplementary Figure 3. Dependence on the thickness of NbSe$_2$. Cavity-modulated superconductivity for devices with NbSe$_2$ thicknesses of (**a**) 6 layers, (**b**) 8 layers, (**c**) 12 layers, and (**d**) 17 layers. The cavity frequency is 0.92 THz, and the Al_2O_3 spacer is 10 nm thick in all four cases. **e**, Cavity-induced T_c enhancement as a function of the layer number of NbSe$_2$.

Supplementary Note 8. Replacement of Al_2O_3 dielectric spacer with HfO_2

We have replaced the Al_2O_3 dielectric spacer with HfO_2. Supplementary Figure 4 shows the measurement of a device with a 10-nm HfO_2 spacer, yielding T_c enhancement consistent with that observed in the Al_2O_3 cases. Reproducing the effect with two chemically distinct dielectric materials strongly disfavors dielectric-specific interfacial effects or associated fabrication artifacts.

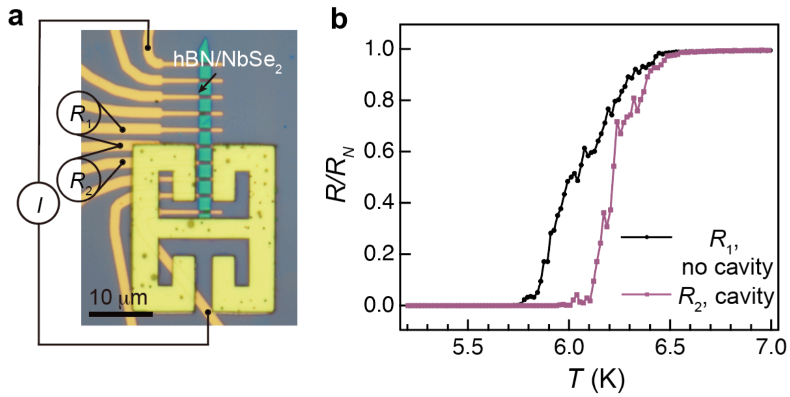

Supplementary Figure 4. Control experiment with HfO_2 spacer. a,**b**, Optical micrograph and cavity-modulated superconductivity for a device with a 10-nm-thick HfO_2 spacer. The cavity frequency is 0.92 THz. The $NbSe_2$ flake has a thickness of 12 layers.

Supplementary Note 9. Ginzburg-Landau theory for the coupled superconductor-cavity system

(1) Cavity renormalization in the Ginzburg-Landau (GL) theory

We consider the effects of the cavity on the superconductor close to the transition. The superconductor is described by the time-dependent Ginzburg-Landau action,

$$S_{\mathrm{SC}} = \int dtd^3x \left[\overline{\psi}(i\partial_t + 2eA_0)\psi - \frac{1}{2m}|D_i\psi|^2 - \alpha|\psi|^2 - (\beta/2)|\psi|^4\right], \tag{S1}$$

$$= \int dtd^3x \left[\overline{\psi}\left(i\partial_t + 2eA^0 + \frac{\Delta}{2m} - \alpha\right)\psi - \frac{ie}{m}A^i\left(\overline{\psi}\partial_i\psi - \psi\partial_i\overline{\psi}\right) - \frac{2e^2}{m}|A|^2|\psi|^2 - \left(\frac{\beta}{2}\right)|\psi|^4\right],$$

where $D_j = \partial_j - i2eA_j$, and in the second line we use that A_j is real. Additionally, we consider fluctuations of the electromagnetic field in the cavity. These are controlled by the Maxwell action,

$$S_{\mathrm{EM}} = \frac{\varepsilon}{2}\int dtd^3x \left[(\partial_t A)^2 - \frac{1}{2\varepsilon\mu}(\nabla \times A)^2\right], \tag{S2}$$

where we use the radiation gauge $A^0 = 0$ in which the vector potential contains longitudinal components. In this gauge, the light–matter coupling can effectively incorporate the density–scalar-potential interaction that appears in the Coulomb gauge, which is expected to dominate over the current-vector-potential interaction in a sub-wavelength cavity[12]. We consider the case where a single mode dominates the coupling to the cavity, with parametrization

$$\vec{A}_c = q(t)\,\phi(\vec{x})\,\hat{e}_y, \tag{S3}$$

where $\phi(\vec{x})$ is the mode function, giving the spatial profile of the cavity mode, $\hat{e}_y$ is the polarization direction, and $q(t)$ is the fluctuating amplitude. Using the mode function properties

$$\nabla^2\phi(\vec{x}) = -\varepsilon\mu\omega_c^2\phi(\vec{x}), \qquad \int d^3x\,\phi^2 = 1, \tag{S4}$$

where ω_c is the cavity frequency, we find that equation (S2) simplifies to

$$S_\mathrm{EM} = \frac{\varepsilon}{2}\int d\,t(\dot{q}^2 - \omega_\mathrm{c}^2 q^2). \tag{S5}$$

In order to calculate the effect of fluctuations on the large-scale physics, we consider the two-point vertex,

$$\Gamma^{(2)}(t,\vec{x},t',\vec{x}') = \frac{i}{\langle\psi(t,\vec{x})\overline{\psi}(t',\vec{x}')\rangle}, \tag{S6}$$

in the presence of interactions. Explicitly,

$$\langle\psi(t,\vec{x})\overline{\psi}(t',\vec{x}')\rangle = \frac{1}{Z[0,0]}\frac{\delta}{i\delta\overline{\eta}(t,\vec{x})}\frac{\delta}{i\delta\eta(t',\vec{x}')}Z[\eta,\overline{\eta}], \tag{S7}$$

with the generating function

$$Z[\eta,\overline{\eta}] = \int \mathcal{D}[\psi,\overline{\psi}]\mathcal{D}q\, e^{i[S_\mathrm{SC}+S_\mathrm{EM}+\int dt d^3x(\overline{\psi}\eta+\overline{\eta}\psi)]}$$

$$= \sum_{m,n,p}\int \mathcal{D}[\psi,\overline{\psi}]\mathcal{D}q\left(\frac{1}{m!\,n!\,p!}\right)\left(-\frac{i\beta}{2}\int|\psi|^4\right)^m\left(\frac{e}{m}\int q\phi\left(\overline{\psi}\partial_y\psi - \psi\partial_y\overline{\psi}\right)\right)^n$$

$$\times\left(-\frac{i2e^2}{m}\int q^2\phi^2|\psi|^2\right)^p \mathrm{e}^{i\int dt\left\{\frac{\varepsilon}{2}\left(\dot{q}^2-\omega_c^2q^2\right)+\int d^3x\left[\overline{\psi}\left(i\partial_t+\frac{\Delta}{2m}-\alpha\right)\psi+\overline{\psi}\eta+\overline{\eta}\psi\right]\right\}}. \tag{S8}$$

The$(m,n,p)=(0,0,0)$ contribution gives the bare propagator,

$$\left\langle\psi(t,\vec{x})\overline{\psi}(t',\vec{x}')\right\rangle_{(0,0,0)}=\frac{i}{i\partial_t+\frac{\Delta}{2m}-\alpha}(t,\vec{x},t',\vec{x}'), \tag{S9}$$

which we represent by a solid line (see Supplementary Fig. 5).

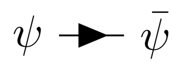

Supplementary Figure 5. Bare ψ propagator.

The $p=1$ contribution gives (see Supplementary Fig. 6)

$$\left\langle-\psi(x)\overline{\psi}(x')i\int_y\frac{2e^2q^2\phi^2|\psi|^2}{m}\right\rangle=$$
$$-i\frac{2e^2}{m}\int d\,t_y d^3y\phi^2(y)\langle q^2(t)\rangle\left\langle\psi(x)\overline{\psi}(y)\right\rangle\left\langle\psi(y)\overline{\psi}(x')\right\rangle, \tag{S10}$$

where we keep only the connected contractions and use the simplified notation $\psi(x)=\psi(t_x,\vec{x})$. The bare propagator for the single photonic mode is

$$\langle\, q(t)\, q(t')\rangle=\frac{i}{\varepsilon(-\partial_t^2-\omega_c^2)}\,, \tag{S11}$$

so that, by Wick rotation,

$$\langle q^2(t)\rangle\rightarrow\int\frac{d\omega}{2\pi}\frac{1}{\varepsilon(\omega^2+\omega_c^2)}=\frac{1}{2\varepsilon\omega_c}. \tag{S12}$$

Substituting this result in equation (S10),

$$\left\langle\psi(x)\overline{\psi}(x')\right\rangle_{(0,0,1)}=$$
$$\frac{ie^2}{\varepsilon m\omega_c}\int\frac{d\omega}{2\pi}e^{-i\omega(t_x-t_{x'})}\int\frac{d^3k}{(2\pi)^3}\frac{d^3k'}{(2\pi)^3}d^3y\phi^2(\vec{y})\frac{e^{ik\cdot(x-y)}}{\omega-\frac{k^2}{2m}-\alpha}\frac{e^{ik'\cdot(y-x')}}{\omega-\frac{k'^2}{2m}-\alpha}. \tag{S13}$$

In general, the mode function destroys translational symmetry. To extract the translation-invariant part, we do a spatial average of this term over the sample volume V_{SC}, which is approximately 2 µm × 25 µm × 8 nm in the experiment. The important result is

$$\frac{1}{V_{\mathrm{SC}}}\int d^3x'\left(\int \frac{d^3k'}{(2\pi)^3}d^3y\phi^2(\vec{y})e^{i[k\cdot(x-y)+k'\cdot(y-x')]}\right) \tag{S14}$$

$$=\int \frac{d^3k'}{(2\pi)^3}\frac{d^3k''}{(2\pi)^3}\tilde{\phi}(k'')\tilde{\phi}(k-k'-k'')e^{ik\cdot(x-x')}\frac{(2\pi)^3\delta(k-k')}{V_{\mathrm{SC}}}. \tag{S15}$$

Inserting this relation in equation (S13), and defining

$$\int \frac{d^3k}{(2\pi)^3}\tilde{\phi}(k)\tilde{\phi}(-k) \simeq \int_{V_{\mathrm{SC}}} d^3x\,\phi^2(\vec{x}) =: \chi_\phi \tag{S16}$$

where the pure number $0<\chi_\phi<1$ gives the fractional overlap of the mode function with the sample. Then we find the tadpole correction

$$\langle\psi(x)\overline{\psi}(x')\rangle_{(0,0,1)} = \frac{ie^2\chi_\phi}{\varepsilon m\omega_{\mathrm{c}}V_{\mathrm{SC}}}\int\frac{d\omega}{2\pi}\frac{d^3k}{(2\pi)^3}\frac{e^{i[k\cdot(x-x')-\omega(t_x-t_{x'})]}}{\left(\omega-\frac{k^2}{2m}-\alpha\right)^2}. \tag{S17}$$

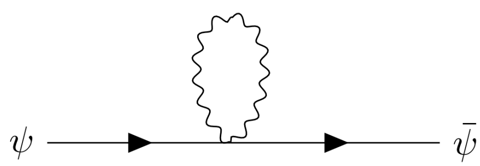

Supplementary Figure 6. Tadpole correction to the propagator.

The final connected diagram that contributes at this order arises from the *n* = 2 term in equation (S8) (see Supplementary Fig. 7),

$$\left\langle\psi(x)\psi(x')\frac{1}{2!}\left(\frac{e}{m}\int q\phi\left(\overline{\psi}\partial_y\psi-\psi\partial_y\overline{\psi}\right)\right)^2\right\rangle$$

$$=\frac{e^2}{m^2}\int d\,t_z d^3z dt_w d^3w\langle q(t_z)q(t_w)\rangle\langle\psi(x)\overline{\psi}(z)\rangle\langle\psi(w)\overline{\psi}(x')\rangle \tag{S18}$$

$$\times[-\phi(z)\left\langle\partial_y\psi(z)\partial_y\left(\phi(w)\overline{\psi}(w)\right)\right\rangle-\phi(z)\phi(w)\langle\partial_y\psi(z)\partial_y\overline{\psi}(w)\rangle$$

$$-\left\langle\partial_y(\phi(z)\psi(z))\partial_y\left(\phi(w)\overline{\psi}(w)\right)\right\rangle-\phi(w)\langle\partial_y(\phi(z)\psi(z))\partial_y\overline{\psi}(w)\rangle],$$

where we are careful to keep the spatial dependence of the mode function arbitrary. Again, we extract the translation-invariant part of this term by averaging over the sample. We then find that

$$\left\langle \psi(x)\overline{\psi}(x')\right\rangle_{(0,2,0)} = -\frac{e^2}{m^2 V_{\mathrm{SC}}}\int \frac{d\omega}{2\pi}\frac{d^3k}{(2\pi)^3}\frac{e^{i[k(x-x')-\omega(t_x-t_{x'})]}}{\left(\omega-\frac{k^2}{2m}-\alpha\right)^2} I(\omega,k;\phi), \qquad (S19)$$

where the remaining loop integral is

$$I(\omega,k;\phi) = \int \frac{d\omega_1}{2\pi}\frac{d^3k'}{(2\pi)^3}\left|\tilde{\phi}(k')\right|^2 \frac{1}{\varepsilon(\omega_1^2-\omega_c^2)}\frac{4k_y^2-4k_yk'_y+k'^2_y}{(\omega-\omega_1)-\frac{(k-k')^2}{2m}-\alpha}. \qquad (S20)$$

We use the reality of the mode function, $\tilde{\phi}(-k)=\tilde{\phi}^*(k)$. Note that, if the mode function is set to be a plane wave with fixed momentum, equation (S20) reduces to the same integral one which one would find by directly applying the Feynman rules to the diagram in Supplementary Fig. 7.

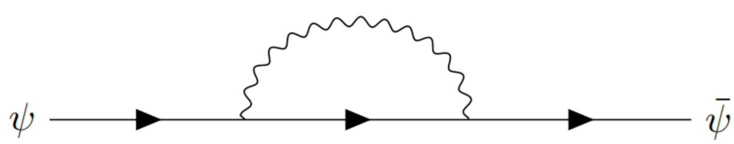

Supplementary Figure 7. Second-order diagram correction to the propagator.

Putting all the terms together, the one-loop vertex is

$$\Gamma^{(2)}(\omega,k) = i\left[\frac{i}{\omega-\frac{k^2}{2m}-\alpha}+\frac{ie^2\chi_\phi}{\varepsilon m\omega_{\mathrm{c}}V_{\mathrm{SC}}}\frac{1}{\left(\omega-\frac{k^2}{2m}-\alpha\right)^2}-\frac{e^2}{m^2V_{\mathrm{SC}}}\frac{I(\omega,k;\phi)}{\left(\omega-\frac{k^2}{2m}-\alpha\right)^2}\right]^{-1} \qquad (S21)$$

$$= \omega-\frac{k^2}{2m}-\alpha-\frac{e^2\chi_\phi}{\varepsilon m\omega_{\mathrm{c}}V_{\mathrm{SC}}}-\frac{ie^2}{m^2V_{\mathrm{SC}}}I(\omega,k;\phi)+O(e^4). \qquad (S22)$$

(2) Cavity loss

We include the broadening of the spectral functions due to cavity loss. The spectral representation of the photon propagator is

$$\frac{1}{\omega^2-\omega_c^2+i\epsilon}=\int d\,\omega'\frac{A(\omega')}{\omega-\omega'+i\epsilon},A(\omega)=\frac{1}{2\omega_c}[\delta(\omega-\omega_c)-\delta(\omega+\omega_c)]. \quad (S23)$$

With finite frequency broadening γ, the spectral function becomes

$$A_\gamma(\omega)=\frac{1}{2\pi\omega_c}\frac{\gamma}{(\omega-\omega_c)^2+\gamma^2}-\frac{1}{2\pi\omega_c}\frac{\gamma}{(\omega+\omega_c)^2+\gamma^2}. \quad (S24)$$

We compute the frequency integral in equation (S20) by displacing the poles of the two propagators in the loop according to the Feynman prescription. After simplifications, we find

$$\int\frac{d\omega_1}{2\pi}\int d\,\omega'\frac{A(\omega')}{\omega_1-\omega'-i\epsilon}\frac{1}{\omega_1-\Omega+i\epsilon}=\frac{i}{2\omega_c}\left[\frac{1}{(\Omega+\omega_c)-i\gamma}-\frac{1}{(\Omega-\omega_c)-i\gamma}\right], (S25)$$

where we use the notation $\Omega(\omega,k)=\omega-\frac{k^2}{2m}-\alpha$. Similarly, the spectral function broadening modifies the tadpole contribution by

$$\langle q^2(t)\rangle\propto\frac{1}{2\omega_c}\rightarrow\frac{1}{2\sqrt{\omega_c^2-\gamma^2}}. \quad (S26)$$

(3) GL coefficients

To obtain the renormalized Ginzburg-Landau coefficients, we consider the long-wavelength, low-frequency expansion of the effective action. To the quadratic level, it is given by

$$\int\frac{d\omega}{2\pi}\frac{d^3k}{(2\pi)^3}\Gamma^{(2)}(\omega,k)\tilde{\phi}(\omega,k)\tilde{\phi}(-\omega,-k),$$
$$\Gamma^{(2)}(\omega,k)=\mathcal{Z}\omega-\frac{k^2}{2m_*}-\alpha_*+O(k^4,\omega^2), \quad (S27)$$

where $\mathcal{Z}$ is a wavefunction renormalization. Expanding equation (S22), we find that

$$\alpha_*=-\Gamma^{(2)}(0,0)=\alpha+\frac{e^2\chi_\phi}{\varepsilon m V_{SC}\sqrt{\omega_c^2-\gamma^2}}+\frac{ie^2}{m^2V_{SC}}I(0,0) \quad (S28)$$

$$= \alpha + \frac{e^2\chi_\phi}{\varepsilon m V_{\mathrm{SC}}\sqrt{\omega_{\mathrm{c}}^2-\gamma^2}}$$

$$+\frac{e^2}{2m^2\omega_{\mathrm{c}}V_{\mathrm{SC}}}\int\frac{d^3k}{(2\pi)^3}\left|\tilde{\phi}(k)\right|^2\frac{k_y^2}{\varepsilon}\left[\frac{1}{(\Omega+\omega_{\mathrm{c}})-i\gamma}-\frac{1}{(\Omega-\omega_{\mathrm{c}})-i\gamma}\right]. \tag{S29}$$

The mode function should be a real solution of the equation $\nabla^2\phi(\vec{x}) = -\varepsilon\mu\omega_{\mathrm{c}}^2\phi(\vec{x})$. The simplest solution, which accommodates both the short-distance variations as well as the damping, is decaying oscillations, which corresponds to the presence of a complex pole in the Fourier transform $\tilde{\phi}(k)$. For simplicity, we assume a single oscillation length and a single decay length. The reality of $\phi(\vec{x})$ implies that $\tilde{\phi}(-k)=\tilde{\phi}(k)^*$, so that a pole at k_{c} is accompanied by a pole at $-k_{\mathrm{c}}^*$. Then, we can evaluate

$$\mathrm{Re}\int\frac{d^3k}{(2\pi)^3}\tilde{\phi}(k)\tilde{\phi}(-k)k_y^2\frac{1}{(\Omega+\omega_{\mathrm{c}})-i\gamma}$$

$$\simeq \mathrm{Re}\int\frac{dk_y}{2\pi}\frac{K^3}{(k_y-k_{\mathrm{c}})(k_y+k_{\mathrm{c}}^*)(k_y+k_{\mathrm{c}})(k_y-k_{\mathrm{c}}^*)}\frac{k_y^3}{(\Omega(k_y)+\omega_{\mathrm{c}})-i\gamma} \tag{S30}$$

$$=\frac{2\pi^2\chi_\phi|k_{\mathrm{c}}|^2\mathrm{Im}(k_{\mathrm{c}})}{\omega_{\mathrm{c}}}\{\frac{1}{\mathrm{Im}(k_{\mathrm{c}})}\mathrm{Re}\left[\left(-\frac{k_{\mathrm{c}}^2}{2m\omega_{\mathrm{c}}}+1-i\frac{\gamma}{\omega_{\mathrm{c}}}\right)^{-1}+\left(-\frac{k_{\mathrm{c}}^{*2}}{2m\omega_{\mathrm{c}}}+1-i\frac{\gamma}{\omega_{\mathrm{c}}}\right)^{-1}\right]$$

$$-\frac{1}{\mathrm{Re}(k_{\mathrm{c}})}\mathrm{Im}\left[\left(-\frac{k_{\mathrm{c}}^2}{2m\omega_{\mathrm{c}}}+1-i\frac{\gamma}{\omega_{\mathrm{c}}}\right)^{-1}-\left(-\frac{k_{\mathrm{c}}^{*2}}{2m\omega_{\mathrm{c}}}+1-i\frac{\gamma}{\omega_{\mathrm{c}}}\right)^{-1}\right]\}, \tag{S31}$$

where in the second line we fixed the normalization K of the mode function in momentum space using equation (S16), which gives $\chi_\phi = \frac{K^3}{16\pi^2|k_{\mathrm{c}}|^2\mathrm{Im}(k_{\mathrm{c}})}$. Note that the presence of a complex pole introduces both the real and imaginary parts of the distribution function in equation (S31). These are symmetric and antisymmetric with respect to the pole, respectively, leading to the asymmetry of $\delta\alpha(\omega_{\mathrm{c}})$ around the peak.

(4) Critical temperature

The superconducting transition corresponds to the appearance of a finite condensate density, $\rho = |\psi_*|^2 = -\frac{\alpha}{\beta} > 0$, so that the critical temperature is defined by the point where α changes sign. Close to the transition,

$$\alpha_0(T_* - T_c) + \delta\alpha = 0 \Rightarrow \delta T_c = T_* - T_c = -\frac{\delta\alpha}{\alpha_0}, \tag{S32}$$

so that, for a generic mode function,

$$\delta T_c = -\frac{e^2 \chi_\phi}{\varepsilon \alpha_0 m V_{SC} \sqrt{\omega_c^2 - \gamma^2}} - \frac{e^2}{2\varepsilon\alpha_0 m^2 V_{SC}\omega_c} \mathrm{Re} \int \frac{d^3k}{(2\pi)^3} \left|\tilde{\phi}(k)\right|^2 k_y^2 \left[\frac{1}{(\Omega + \omega_c) - i\gamma} - \frac{1}{(\Omega - \omega_c) - i\gamma}\right]. \tag{S33}$$

For our case of a single k_c we apply equation (S31). Using the rescaled quantities

$$\overline{V}_{SC} = \frac{V_{SC}}{1\ \mu m^3}, \qquad \overline{\alpha}_0 = \frac{\alpha_0}{10^{-5}\mathrm{eV/K}}, \qquad \overline{x} = \frac{2\pi/\mathrm{Re}[k_c]}{1\ \mu m}, \qquad \overline{y} = \frac{2\pi/\mathrm{Im}[k_c]}{1\ \mu m}, \tag{S34}$$

We find that $(2\pi)^3 \varepsilon \overline{\alpha}_0 \overline{V}_{SC} \overline{K}^{-3} = 19.8$, $\overline{x} = 0.015, \overline{y} = 0.479$, where $\overline{K} = 1\ \mu m \times K$ and K are defined under equation (S31). Accordingly, we present the theoretical prediction of $\delta T_c / T_c$ in Fig. 3 of the main text.

Supplementary Note 10. Extraction of *Q* and its impact on *T*c modulation

As illustrated in equation (2) in the main text, cavity quality factor $Q = \frac{\omega_c}{2|\gamma|}$ can influence the critical temperature through the attenuation γ. Its role is important due to the finite loss in THz cavities[13]. Supplementary Figure 8 compares the theoretical results for different Q values (dashed lines), showing that Q crucially determines the peak width and amplitude, and thus the maximum T_c enhancement.

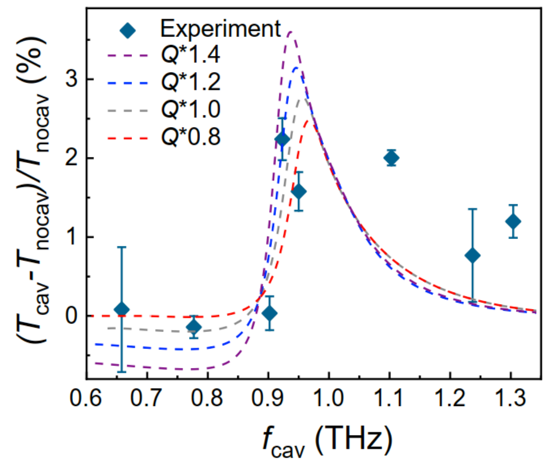

Supplementary Figure 8. Frequency-dependent superconductivity enhancement for different *Q* values. Dashed lines represent the theoretical prediction curves for the quality factor Q rescaled by factors of 1.4, 1.2, 1.0 and 0.8, respectively, while all other parameters are kept fixed.

The quoted value $Q \approx 11$ is inferred from fitting the experimental data in Supplementary Fig. 8. Q represents the effective cavity linewidth, where dissipation is incorporated via a frequency broadening γ, with $Q = \frac{\omega_c}{2|\gamma|}$. $\gamma(\omega_c)$ is modeled phenomenologically as $\gamma(\omega_c) = a\omega_c + b$, with fitted parameters $a \approx 1.95$, $b \approx -2.48$ to reproduce the measured T_c modulation (Supplementary Fig. 8). This yields a representative value $Q \approx 11$ at around 1.3 THz.

Supplementary Note 11. Influence of the dielectric environment on T_c modulation

Influence of the dielectric environment on T_c modulation manifests in three ways: (1) The vacuum field fluctuation amplitude can be estimated as $E = \sqrt{\hbar\omega_c/2\varepsilon_0\varepsilon_s V_{\mathrm{eff}}}$. Thus, the dielectric environment modifies the cavity field amplitude by changing the effective permittivity ε_s and reshaping the effective volume V_{eff}, thereby tuning the magnitude of T_c enhancement; (2) The resonant frequency of the LC resonator is set by its effective inductance L_{eff} and capacitance C_{eff}: $f \approx \frac{1}{2\pi\sqrt{L_{\mathrm{eff}}C_{\mathrm{eff}}}}$. The dielectric environment enters the resonant frequency via $C_{\mathrm{eff}} \propto \varepsilon_{\mathrm{eff}}$. Therefore, changing the dielectric environment shifts the cavity resonant frequency as $f \sim 1/\sqrt{\varepsilon_{\text{eff}}}$; (3) One of loss channels that limit the quality factor Q is dielectric loss, which is determined by the dielectric environment. A low-loss dielectric environment increases the quality factor, and generally enhances the effective light-matter coupling, thereby increasing the magnitude of the cavity-enhanced superconductivity.

Substrate and capping materials form the dielectric environment, which modifies multiple cavity parameters, including the permittivity ε_s, effective volume V_{eff}, cavity resonant frequency f, and quality factor Q, thereby changing the measured T_c enhancement. Specifically, increasing the dielectric constant or thicknesses of the capping layers increases ε_s and V_{eff}, which reduces cavity field strength and decreases ΔT_c. Moreover, a larger permittivity tends to redshift the resonant frequency of the maximum T_c enhancement. Introducing a lossy dielectric material suppresses the light-matter coupling and reduces the measured T_c enhancement.

Supplementary Note 12. Discussion based on the sub-wavelength cavity theory

There has been substantial debate in sub-wavelength cavity theory[12,14-17], regarding whether the interaction should be described as a current-vector-potential interaction or a density-scalar-potential interaction, and whether one can legitimately "import" Fabry-Pérot intuition by introducing a mode-volume compression factor. In our model, the cavity-matter interaction is consistent with the conclusion in Ref. [12]. More rigorously, both the density-scalar-potential interaction and the current-vector-potential interaction in the Coulomb gauge $\nabla \cdot \vec{A} = 0$ should be present. To incorporate both contributions in a transparent way, we instead work in the radiation gauge, where $\delta\phi(x,t) = 0$. In this formulation, the scalar potential is decomposed into an electrostatic part and a dynamical part, $\phi(x,t) = \bar{\phi}(x) + \delta\phi(x,t)$, while the vector potential contains both transverse and longitudinal components ($\vec{A}_\perp$ and $\vec{A}_\parallel$, respectively).

For finite-frequency cavity modes, the coupling between the longitudinal component of the vector potential and the current in the radiation gauge is equivalent to the density-scalar-potential interaction in the Coulomb gauge. As a result, the radiation gauge naturally incorporates both longitudinal and transverse electromagnetic fluctuations in the diagrammatic treatment. In other words, both charge and current fluctuations are consistently included in our theory.

The purely electrostatic term $\bar{\phi}(x)\rho(\mathrm{x})$ may be neglected since the field strength of the screening correction is much weaker than the dynamical cavity field, as estimated in Supplementary Note 6(1). This separation is further supported by the agreement between our theory and the experimental data in the frequency dependence of T_c enhancement (Fig. 3d of the main text).

We note that in the deep sub-wavelength regime, one should use the volume from the full electromagnetic environment simulation to avoid introducing artificial mode-volume compression factor as we did. The mode confinement is far below the diffraction limit constrained by the actual device geometry, without rescaling the vacuum field amplitude.

Supplementary Note 13. Discussion based on the microscopic picture of polaritonic coupling

A microscopic picture of polaritonic coupling has been introduced to the modulation of superconductivity[16,18], where the underlying physics is governed by Hopfield-type polaritonic coupling between well-identified bosonic modes.

In our case, the analysis is formulated at the level of a Ginzburg–Landau (GL) description appropriate to the vicinity of the superconducting transition accessed in the experiment. Within this framework, cavity vacuum fluctuations renormalize the GL coefficients through one-loop processes leading to an enhancement of T_c. The experimentally observed effect is thus well explained by a thermodynamic renormalization near the phase transition.

It is natural to speculate that, at a more microscopic level, the cavity may couple preferentially to certain phonons in the hBN substrate or the superconductor, thereby inducing polaritons. If such polaritons exist, they could influence superconductivity.

However, the situation is subtle in the case of the superconductor $NbSe_2$. $NbSe_2$ is a complex material characterized by anisotropic and strongly momentum-dependent electron–phonon coupling, where superconductivity is believed to be supported by multiple phonon branches rather than a single well-defined pairing mode. In this context, light–matter hybridization with the split-ring resonator is not expected to manifest as a single isolated polariton resonance, but rather as a distributed spectrum involving several weakly hybridized lattice fluctuations. Additionally, the material has multiple Fermi-surface pockets, anisotropic superconducting gaps, and coexisting CDW order. These microscopic details make it difficult to establish a direct one-to-one connection between a specific polaritonic coupling and the observed T_c enhancement without a full momentum- and band-resolved pairing analysis, which is beyond the scope of the present work. The GL analysis, on the other hand, captures the near-T_c thermodynamic effect of the cavity through the renormalization of the superconducting free-energy coefficients. A fully microscopic identification of the polaritonic coupling in $NbSe_2$ would require future studies.

Supplementary Note 14. Strategies for amplifying cavity-enhanced superconductivity

Within our microscopic framework, the cavity-induced superconductivity enhancement scales with the effective dimensionless coupling, which can be further enhanced from both the material and cavity sides:

(1) Material side strategies

The effect depends on how "susceptible" the electronic system is to the cavity field. In this respect, low-density, highly tunable 2D superconductors (e.g., gated MoS_2, twisted graphene, $LaAlO_3/SrTiO_3$ interface) with small Fermi energies and strong interaction effects can produce a large change in the coupling strength and thus in T_c. Tuning density via gating can move the system into regimes (e.g., near van Hove singularities, Lifshitz transitions) where the electronic response to the cavity field is maximized. High-temperature superconductors (e.g., $Bi_2Sr_2CaCu_2O_{8+\delta}$, FeSe) are also promising for achieving significant enhancement of T_c. The large absolute T_c means that even a fewpercent enhancement corresponds to a large absolute shift. More interestingly, materials such as FeSe or cuprates host additional low-energy collective modes (e.g., spin or pairing fluctuations) that can hybridize with the cavity field, providing additional enhancement channels beyond conventional BCS-like systems.

(2) Cavity side strategies

Another route to enhance T_c is to enhance the cavity fluctuations. Our calculation based on Ginzburg-Landau theory shows that this can be achieved for small cavity volumes and low permittivity of the medium. Both factors are well known to enhance the amplitude of electromagnetic vacuum fluctuations and have been widely exploited across different cavity-QED platforms. Second, the cavity frequency should satisfy the resonance condition, where the cavity-photon energy matches the energy of the condensate at the momentum gained from the photons. Finally, achieving a high-quality factor (Q) can further strengthen the coupling. A low-loss dielectric environment increases the quality factor, and generally enhances the effective light-matter coupling, thereby increasing the magnitude of the cavity-enhanced superconductivity.

References:

1. Appugliese, F. *et al.* Breakdown of topological protection by cavity vacuum fields in the integer quantum Hall effect. *Science* **375**, 1030-1034 (2022). https://doi.org/10.1126/science.abl5818
2. Enkner, J. *et al.* Tunable vacuum-field control of fractional and integer quantum Hall phases. *Nature* **641**, 884-889 (2025). https://doi.org/10.1038/s41586-025-08894-3
3. Xu, C.-Z. *et al.* Experimental and theoretical electronic structure and symmetry effects in ultrathin $NbSe_2$ films. *Phys. Rev. Mater.* **2**, 064002 (2018). https://doi.org/10.1103/PhysRevMaterials.2.064002
4. Calandra, M., Mazin, I. I. & Mauri, F. Effect of dimensionality on the charge-density wave in few-layer 2H-$NbSe_2$. *Phys. Rev. B* **80**, 241108 (2009). https://doi.org/10.1103/PhysRevB.80.241108
5. He, R. *et al.* Interlayer breathing and shear modes in $NbSe_2$ atomic layers. *2D Mater.* **3**, 031008 (2016). https://doi.org/10.1088/2053-1583/3/3/031008
6. Xi, X. *et al.* Strongly enhanced charge-density-wave order in monolayer $NbSe_2$. *Nat. Nanotechnol.* **10**, 765-769 (2015). https://doi.org/10.1038/nnano.2015.143
7. Xi, X. *et al.* Ising pairing in superconducting $NbSe_2$ atomic layers. *Nat. Phys.* **12**, 139-143 (2016). https://doi.org/10.1038/nphys3538

8. Tao, H. *et al.* Highly flexible wide angle of incidence terahertz metamaterial absorber: Design, fabrication, and characterization. *Phys. Rev. B* **78**, 241103 (2008). https://doi.org/10.1103/PhysRevB.78.241103
9. Robinson, J. T., Manolatou, C., Chen, L. & Lipson, M. Ultrasmall mode volumes in dielectric optical microcavities. *Phys. Rev. Lett.* **95**, 143901 (2005). https://doi.org/10.1103/PhysRevLett.95.143901
10. Zhang, Y. *et al.* High-temperature superconductivity with zero resistance and strange-metal behaviour in $La_3Ni_2O_{7-\delta}$. *Nat. Phys.* **20**, 1269-1273 (2024). https://doi.org/10.1038/s41567-024-02515-y
11. Wagenknecht, M. *et al.* Phase diagram of the electron-doped $La_{2-x}Ce_xCuO_4$ cuprate superconductor from Andreev bound states at grain boundary junctions. *Phys. Rev. Lett.* **100**, 227001 (2008). https://doi.org/10.1103/PhysRevLett.100.227001
12. Andolina, G. M. *et al.* Amperean superconductivity cannot be induced by deep subwavelength cavities in a two-dimensional material. *Phys. Rev. B* **109**, 104513 (2024). https://doi.org/10.1103/PhysRevB.109.104513
13. Zhang, Q. *et al.* Collective non-perturbative coupling of 2D electrons with high-quality-factor terahertz cavity photons. *Nat. Phys.* **12**, 1005-1011 (2016). https://doi.org/10.1038/nphys3850
14. Riolo, R. *et al.* Tuning Fermi liquids with polaritonic cavities. *Proc. Natl. Acad. Sci. U.S.A.* **122**, e2407995122 (2025). https://doi.org/doi:10.1073/pnas.2407995122
15. Andolina, G. M. *et al.* Quantum electrodynamics of graphene Landau levels in a deep-subwavelength hyperbolic phonon-polariton cavity. *Phys. Rev. Res.* **8**, 023044 (2026). https://doi.org/10.1103/69jg-sq8r
16. Riolo, R. *et al.* Polariton-induced superconductivity in two-dimensional metals. arXiv:2511.00608 (2025). <https://ui.adsabs.harvard.edu/abs/2025arXiv251100608R>.
17. Schlawin, F., Cavalleri, A. & Jaksch, D. Cavity-mediated electron-photon superconductivity. *Phys. Rev. Lett.* **122**, 133602 (2019). https://doi.org/10.1103/PhysRevLett.122.133602
18. Keren, I. *et al.* Cavity-altered superconductivity. *Nature* **650**, 864-868 (2026). https://doi.org/10.1038/s41586-025-10062-6